

# FMCW BASED MIMO IMAGING RADAR

**D. Patrick**

Guidance Navigation Ltd, C2, Knowl Piece, Wilbury Way, Hitchin SG4 0TY, United Kingdom

**Y. Huang, P.V. Brennan**

Department of Electronic & Electrical Engineering, University College London, Torrington Place, London WC1E 7JE, United Kingdom

**Abstract –**

There are a number of potential applications for low cost short range phased array radar sensors: ship bumpers, large vehicle sensors and level crossing obstacle detection for example. Phased arrays have the benefit of reduced size and the elimination of moving parts compared with more traditional rotating antenna systems. Another potential benefit is that the image update rate can be orders of magnitude faster than that for mechanically steered radars. Phased array radars have been developed for many years but the high cost has traditionally limited their use to high performance military radars. Co-located Multiple-In Multiple-Out (MIMO) systems have the potential to mimic the performance of more expensive traditional systems but with substantially lower cost. Such an example system is presented here using 4 transmit elements and 16 receivers to synthesize a 64 virtual element phased array. An integrated 24GHz sensor has been made and field trials performed which confirm the range and angle resolution performance.

Key words: Radar Systems, MIMO Systems, Phased Array Radar, FMCW, Imaging Radar.

## 1 INTRODUCTION

Phased array radar employs a group of antennas to radiate and receive electromagnetic signals, the phases of which are adjusted so that the radar is able to scan or steer across the desired directions while suppressing the responses from other directions. This technique has been in place for many years and is now a reliable and popular option for imaging radar. While the mechanism of phased array is well known, the recent combination of phased array with the multiple-input/multiple-output (MIMO) concept [1] has led to an emerging area where lower cost and higher performance can be achieved simultaneously, making MIMO phased array radar an attractive candidate for short range imaging applications.

Basic phased array radar resolves directions of radar echo from passive targets by means of beam-forming techniques, whose angular resolution is limited by the relative size of the array to the signal wavelength [2]. In order to attain high angular resolution and adequate imaging quality, the phased array needs to be relatively large, but the spacing between elements is limited to half a wavelength to avoid grating lobes. Consequently, a large number of antenna elements in the array are required to build a larger array, which adds to the system complexity. Resolution beyond this limit can be achieved with advanced superresolution array processing methods [3-5], which increases the computation load and processing time. On the other hand, a MIMO arrangement of phased array antenna elements provides another possibility for achieving higher resolution with fewer elements.

This paper presents such a novel MIMO phased array radar system that can be built with conventional off-the-shelf components. The detailed system design including architecture, antenna array, and signal model are given in the Section 2. By deramping the frequency modulated continuous wave (FMCW) signals, the proposed radar system is able to digitize received signals at a relatively low sampling rate and thus the imaging processing is simplified. A prototype system of this design has been developed and the initial experimental imaging results are presented in Section 0.

## 2 MIMO PHASED ARRAY RADAR SYSTEM DESIGN

As implied by its name, MIMO radar consists of multiple antenna elements in both signal transmission and reception. For MIMO radar with  $M_t$  transmit (TX) elements and  $M_r$  receive (RX) elements, there are  $M_t \times M_r$  distinct propagation channels from the TX array to the RX array. If the transmitting source (TX channel) of the received signals can be identified at the RX array, a virtual phased array of  $M_t \times M_r$  elements [6] can be synthesized with only  $M_t + M_r$  antenna elements. Diversity of the TX channels can be achieved by employing time division multiplexing, frequency division multiplexing, spatial coding, and orthogonal waveforms. The virtually formed phased array can be designed to produce the desired pattern by arranging the placements of the TX and RX elements in an appropriate way [7;8].

### 2.1 ANTENNA ARRAY ARCHITECTURE

The MIMO phased array radar proposed in this paper consists of a sparsely separated RX array in the middle and two groups of TX elements surrounding the RX array. Figure 1 shows an example array with 4 TX and 16 RX antenna elements, synthesizing a uniform linear array (ULA) of 64 virtual elements. Placement of the physical TX and RX antenna elements, as well as the resultant virtual array, is illustrated by Figure 1.

This is a symmetrical linear arrangement of the TX and RX elements, with some vertical offset between the TX array and the RX array for reduced coupling. Note the coordinates of the TX elements as  $x_i^{Tx}$ ,  $i=1, 2, 3, 4$ , and the coordinates of the RX elements as  $x_j^{Rx}$ ,  $j=1, 2, \dots, 16$ . By arranging the TX elements and RX elements in the way shown by Figure 1, a total of  $M_t \times M_r = 64$  distinct virtual elements can be formed. If the far field condition is met [9], the signal propagation from a TX elements  $x_i^{Tx}$  to a point scatterer  $\mathbf{p}$  plus reflection path from  $\mathbf{p}$  to RX elements can be approximated by the return path between the corresponding virtual element  $x_{ij} = (x_i^{Tx} + x_j^{Rx})/2$ , and the scatterer  $\mathbf{p}$ :

$$P_{ij}(\mathbf{p}) = |\mathbf{p} - x_i^{Tx}| + |\mathbf{p} - x_j^{Rx}| \approx 2|\mathbf{p} - x_{ij}| \quad (1)$$

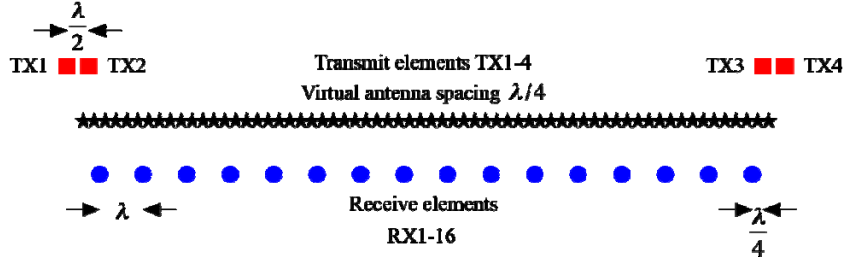


**Figure 1, Illustration of the 20-element MIMO radar topology developed in this work.**

The resultant 64 virtual elements synthesized from the 20 elements shown in Figure 1 are distributed along the middle line (stars in black) between the TX and the RX array.

The rule for designing such a MIMO array with non-overlapping equally spaced elements is simple: If the desired virtual element spacing  $d$  is given, the interelement spacing in either group of the TX array needs to be  $d_t = 2d$ , the interelement spacing in the RX array shall be  $d_r = M_t d$ , and the gap between each  $M_t/2$  element TX group and the edge element of the RX array,  $d_{tr}$ , is equal to  $d$ . By fulfilling these requirements, a virtual ULA of  $M_t \times M_r$  elements separated by  $d$  can be formed in signal processing. The physical length of this MIMO array is  $(M_t M_r + M_t - 2)d$ , and the length of the virtual array is  $(M_t M_r - 1)d$ .

As for the example in the Figure 1, elements in the RX array are separated by  $\lambda$ . The TX array is divided into two groups of two elements, with spacing of  $0.5\lambda$  in each group, placed at both sides of the RX array. The resulting virtual element spacing is therefore  $0.25\lambda$ , which fulfils the grating-lobe-free requirement for this kind of MIMO phased array.

## 2.2 FMCW SIGNAL MODEL

The TX array elements transmit a frequency-modulated continuous wave (FMCW) chirp signal, which can be modelled as:

$$s(t) = \exp[j(2\pi f_c t + \pi k t^2)]; \quad -T_c/2 \leq t \leq T_c/2 \quad (2)$$

where  $T_c$  is the chirp duration,  $f_c$  is the carrier frequency, and  $k$  is the chirp rate defined by the chirp sweeping bandwidth divided by the chirp duration.

$$k = \pm B/T_c \quad (3)$$

Positive chirp rate  $k$  represents up-chirp and negative  $k$  stands for down-chirp.

Assuming that the far field condition is fulfilled, the return delay between a virtual element at  $x_{ij}$  and a scatterer at range  $R$  and angle  $\theta$  (with respect to boresight) can be expressed as

$$\Delta t_{ij} = \frac{2R}{c} + \frac{2x_{ij} \sin \theta}{c} \quad (4)$$

Therefore, the received signal  $r_{ij}(t)$  at element  $x_{ij}$  is a delayed and attenuated version of the transmitted chirp defined in the Eq. (2)

$$r_{ij}(t) = A \cdot s(t - \Delta t_{ij}) \quad (5)$$

where  $A$  represents the combined effect of propagation loss and antenna gains, assuming time-invariance and equal amplitude at each element in this case.

The received chirp signals at the RX array are then processed using a deramp technique, which involves multiplying (with a mixer) the received signal with the transmitted chirp replica, followed by low-pass filtering [10], which process can be modelled as

$$\begin{aligned} u_{ij}(t) &= r_{ij}^*(t)s(t) \\ &= [A \cdot s^*(t - \Delta t_{ij})] \cdot s(t) \\ &= A \cdot \exp[j(2\pi k \Delta t_{ij} t - \pi k \Delta t_{ij}^2 + 2\pi f_c \Delta t_{ij})] \end{aligned} \quad (6)$$

As can be seen, both the range and bearing information are included in the result from the deramp processing given in the Eq. (6).

Firstly, deramping the received signals effectively converts time delay into the frequency domain, as indicated by the frequency term of the deramp result,  $2\pi k \Delta t_{ij} t$ . Frequencies of the deramped signals from the  $j_{\text{th}}$  RX element for the  $i_{\text{th}}$  TX transmit channel are defined by

$$f_{ij} = k \Delta t_{ij} \approx 2k R/c \quad (7)$$

Apparently  $\Delta t_{ij}$  is dominated by  $2R/c$  under far field conditions, and thus is a constant value along all the virtual channels. More importantly, this frequency value is directly proportional to the range  $R$ , allowing the system to retrieve the range information from a simple FFT analysis. Every frequency sample in the frequency domain represents a specific range bin that is linearly proportional to its frequency by  $c/2k$ . Therefore, the range resolution is limited by the frequency resolution, which is inverse to the chirp duration  $T_c$ . It can be found that the range resolution is defined by the bandwidth of the transmitted chirp:

$$\Delta R = \frac{c}{2k} \frac{1}{T_c} = \frac{c}{2B} \quad (8)$$

For example, a chirp bandwidth of 200MHz gives a range resolution of 0.75m.

Secondly, the phase term in Eq. (6) reflects the arrival angle of the echo, which can be found by beamforming with the appropriate steering vectors.

The phase term in Eq. (6) contains a linear  $2\pi f_c \Delta t_{ij}$ , and a squared component  $\pi k \Delta t_{ij}^2$  of the delays. It shall be noted that, for a scatterer within the detectable range of the radar, the squared component is nearly constant for all the virtual channels. The deramped phase term can therefore be expressed as the sum of a phase component dependent on the element coordinates and a constant dependent on the scatterer range.

$$\begin{aligned}
 \varphi &= 2\pi f_c \Delta t_{ij} - \pi k \Delta t_{ij}^2 \\
 &= 2\pi f_c \frac{2x_{ij} \sin \theta}{c} + 2\pi f_c \frac{2R}{c} - \pi k \Delta t_{ij}^2 \\
 &= 4\pi \frac{x_{ij} \sin \theta}{\lambda} + C
 \end{aligned} \tag{9}$$

There are  $M_t M_r$  deramped results in the form of Eq. (6). The steering vectors that can be used to resolve the relative angle of the scatterer are given by the Kronecker product of the steering vector for the TX array and the steering vector of the RX array. The transmitting steering vector is written as

$$a_i^{Tx}(\theta) = \exp\left(-j2\pi \frac{x_i^{Tx} \sin \theta}{\lambda}\right); i = 1, 2, \dots, M_t \tag{10}$$

While the receiving steering vector is

$$a_j^{Rx}(\theta) = \exp\left(-j2\pi \frac{x_j^{Rx} \sin \theta}{\lambda}\right); j = 1, 2, \dots, M_r \tag{11}$$

Given that  $x_{ij} = (x_i^{Tx} + x_j^{Rx})/2$ , the steering vector for the virtual array is thus

$$\begin{aligned}
 a_{ij}(\theta) &= a_i^{Tx}(\theta) \otimes a_j^{Rx}(\theta) \\
 &= \exp\left[-j2\pi \frac{(x_i^{Tx} + x_j^{Rx}) \sin \theta}{\lambda}\right] \\
 &= \exp\left[-j4\pi \frac{x_{ij} \sin \theta}{\lambda}\right]
 \end{aligned} \tag{12}$$

where  $i = 1, 2, \dots, M_t$ , and  $j = 1, 2, \dots, M_r$ . As can be seen, it is in the negative form of the first phase component given by Eq. (9). Subsequently, beamforming of the MIMO array signals can be regarded as synthesizing the received signals with the two-way steering vector, Eq. (12), generated from the coordinates of the virtual elements.

For a given range  $R = cf/2k$ , computed by Eq. (7), the azimuth profile can be found by

$$P(\theta) = \sum_{i=1}^{M_t} \sum_{j=1}^{M_r} \mathbf{U}(f) \cdot a_{ij}(\theta) \quad (13)$$

where  $\mathbf{U}(f)$  is the spectrum of the deramp signals given by Eq. (6).

The angular resolution  $\Delta\theta$  in radians at a given angle  $\theta$  from beamforming is dependent on the effective aperture  $A_e$  of the virtual array:

$$\Delta\theta = \frac{\lambda}{2A_e} = \frac{\lambda}{2(M_t M_r - 1)d \cdot \cos(\theta)} \quad (14)$$

Note that the minimum resolution is at boresight when  $\theta=0$  ( $\cos(\theta) = 1$ ) and the resolution is doubled at an angle of  $60^\circ$  ( $\cos(\theta) = 0.5$ ). Also, if the virtual elements are spaced at  $\lambda/4$  then the angular resolution is fixed by the number of virtual elements and is frequency independent; at boresight, the above equation simplifies to:

$$\Delta\theta = \frac{2}{(N_v - 1)}. \text{ Where } N_v \text{ is the number of virtual elements.}$$

The table below gives some examples of the boresight angular resolution with the number of elements:

Number of Virtual Elements	8	16	32	64
Boresight Angular Resolution (Degrees)	16	7.6	3.7	1.8

The cross range resolution for a position  $(R, \theta)$  can be approximated by the product of angular resolution and the range:

$$\delta R \approx \Delta\theta \cdot R = \frac{\lambda R}{2(M_t M_r - 1)d \cdot \cos(\theta)} \quad (15)$$

The model for using the FMCW signal with the proposed MIMO array for image processing has been summarized in this section. It has shown that a 2-D image can be obtained from the received  $M_t M_r$  channels of samples, by performing Eq. (13) for the full detection range. The range resolution and the angular resolution are given by Eq. (8), and Eq. (14) respectively.

## 2.3 TRANSMIT DIVERSITY BY SWITCHING

In order to synthesize the total number of  $M_t M_r$  MIMO channels, the signal processing shall be able to differentiate the TX channels and separate the time samples according to their originating TX sources. A simple yet reliable method is time division; switching the TX channels on or off for radiation at different time slots.

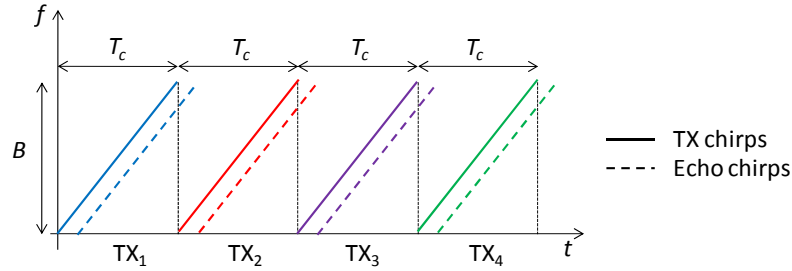


**Figure 2, Transmission scheme for 4-TX elements array**

Consider the 4 TX and 16 RX array given in the Figure 1, with the switching TX scheme the TX elements are activated in turn by a four-way RF switch while the RX elements are receiving microwave signals in parallel and synchronously.

The transmission scheme for this case is given in a time-frequency diagram in Figure 2, which shows the frequency sweeping characteristics of both transmitted and reflected chirps over time in the time slots for the four TX channels.

Reception of signals for the four slots makes a cycle of “scan”. The total  $M_t M_r$  channels of signals are found and an image can be produced when the reflected signals from all the TX slots are received. If the chirp duration is designed to be much longer than the two-way propagation delay corresponding to the furthest detection range ( $\tau = 2R_{max}/c \ll T_c$ ), the range and angle information carried by the received signals can be retrieved at the resolutions defined by Eq. (8) and (14).

Longer chirp duration is usually desirable as it not only ensures the designed resolution but also delivers greater energy to the scatterer, and thus increases the received echo power. However, the chirp duration of FMCW radar is also limited by other practical conditions.

Firstly, the conventional limit on chirp duration due to the target acceleration also applies to this MIMO design. It is defined that the change of radian frequency  $\Delta f_d$  over one chirp duration,  $T_c$ , should not be greater than the frequency resolution  $1/T_c$ , as otherwise the



measurement of the scatterer will be blurred and a false phantom target will appear besides the real target. This condition suggests an upper bound for the chirp duration, noted as  $T_S$ .

The Doppler frequency resulting from target movement at the speed of  $v$  can be modelled as:

$$f_d = \frac{2}{\lambda} v \quad (16)$$

If the target is accelerating, this frequency term will vary too. According to the condition discussed above, the change of Doppler frequency within one chirp duration shall be smaller than the frequency resolution:

$$\Delta f_d = \frac{2}{\lambda} \frac{dv}{dt} T_c = \frac{2a}{\lambda} T_c \leq \frac{1}{T_c} \quad (17)$$

where  $a$  is the acceleration rate of the target. Eq. (16) therefore sets the upper bound on the chirp duration by

$$T_S < \sqrt{\frac{\lambda}{2a_{max}}} \quad (18)$$

where  $a_{max}$  is the maximum possible acceleration of a target that the system is trying to detect.

However, it is not usually the most significant restriction in case of switching transmission MIMO radar, as the upper bound set by the target acceleration is normally looser than that given by the target velocity.

In terms of the switching transmission scheme, since imaging of the environment requires full reception of all  $M_t$  slots of signals, it practically induces a physical relationship between the velocity of a target and the chirp duration. That is, from the first TX slot until the last TX slot, the movement of a target shall not exceed a nominal quarter wavelength, to maintain coherent beamforming. The acceptable average target velocity  $v$  is therefore defined by

$$(M_t - 1) \cdot T_c \cdot v < \lambda/4 \quad (19)$$

which sets an upper bound for the chirp duration as

$$T_M < \frac{\lambda}{4(M_t - 1) \cdot v} \quad (20)$$

To compare these two bounds, let us consider a maritime example where a ship target is moving at the speed of  $v=20$  m/s, with acceleration of  $a=10$  m/s<sup>2</sup>. To image it properly, the maximum chirp durations restricted by Eq. (18) and Eq. (20) are 40 ms and 0.135 ms respectively. It is obvious that the condition derived from Eq. (20) is much stricter. Therefore, compared to conventional single pulse radar, the proposed MIMO radar using switching transmission scheme is constrained by the Eq. (20) to use shorter chirp duration, which results in less power being transmitted and thus reduced radar detection range.

Since the energy carried by a radar signal is proportional to its duration, and the two-way path loss for point targets is proportional to range to the power of four, the reduction in radar detection range caused by shorten chirp duration can be estimated by

$$\frac{R_M}{R_S} \propto \left( \frac{M t * T_M}{T_S} \right)^{1/4} \quad (21)$$

where  $T_M$  and  $R_M$  are maximum chirp duration and maximum detection range for the switched-TX MIMO radar design, while  $T_S$  and  $R_S$  are corresponding maximum figures for single pulse radar.

Consider the example discussed above, where  $T_M=0.135$  ms while  $T_S=40$  ms, the maximum detection range for the switching TX MIMO radar is about a third of that for the single pulse radar.

$$R_M = 0.34 \cdot R_S \quad (22)$$

That is to say, the simplicity and high-quality inter-channel isolation provided by the switching TX scheme are obtained by sacrificing the tolerable target velocity and maximum radar detection range. If this trade-off is not affordable, orthogonal transmission schemes can be consider, where new issues such as isolation between TX channels and raised noise floor may occur.

## 2.4 SYSTEM ARCHITECTURE

The system architecture is illustrated in Figure 3 below.

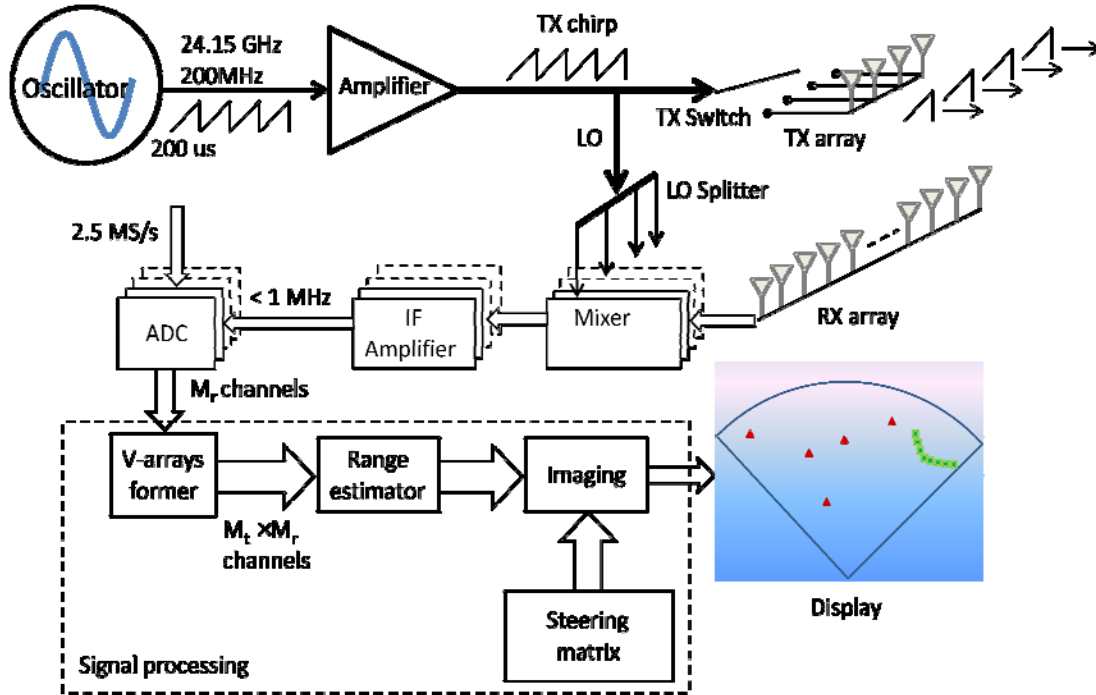


Figure 3, Block diagram of the MIMO phased array radar system

The chirp signal is fed to a four-way RF switch to the 4 TX elements. The switch is programmed to connect one TX element each time sequentially so a full “scan” lasts for  $4 \times 200 \mu\text{s} = 800 \mu\text{s}$  assuming we use a chirp time of  $200 \mu\text{s}$ . The chirp rate can be varied if required to optimise the sensor for the operating range and the expected velocity of the targets.

Echo signals are received by the 16 RX elements simultaneously and deramp processing is applied directly beyond reception of the signals by means of an RF mixer, which mixes the transmitted chirp with the received echoes and producing IF signals whose frequencies are proportional to range of targets (as shown by Eq. (7)).

The IF signals are firstly high-pass filtered to compensate for the range dependant propagation loss before being sampled simultaneously by a 16-channel ADC at a rate of at least  $2.5 \text{ MS/s}$ .

In the digital signal processing, the 16 channels of data are firstly reorganized into 64 channels of echoes and a Fast Fourier transform (FFT) is applied along all the 64 channels of data so that the range information can be resolved using Eq. (7). The steering matrix defined by Eq. (12) is pre-calculated and used to resolve the bearing information from the FFT results. Supperresolution techniques (e.g. MUSIC) can also be used in either range or azimuth profile in order to achieve even better image quality at the cost of longer processing time.

As described previously, for 64 virtual elements the angular resolution at boresight is approximately  $1.8^\circ$ . The cross range resolution, given in Eq. (15), is a function of the distance and a few examples have been listed in Table 1 below.

**Table 1 Cross range resolution at various ranges**

Distance	20 m	50 m	100 m	200 m
Cross range resolution	0.64 m	1.59 m	3.18 m	6.36 m

### 3 FIELD TRIAL RESULTS WITH THE PROTOTYPE SYSTEM

#### 3.1 Prototype System

A 24GHz prototype MIMO sensor has been designed and built as shown in the Figure below.



**Figure 4, Prototype 24GHz sensor.**

The sensor is approximately 26cm by 20cm and 6cm deep and includes the RF, simultaneous sampling and digital signal processing. The lower patches are the transmit antennas with two polarisations and the upper window contains the 16 off receive patch antennas (two patches per antenna).

To examine the performance of the MIMO array radar, the prototype system has been tested in field trials and the results show good agreement between the theoretical analyses and the measured images.

### 3.1 IMAGE RESOLUTION

The images below show the sensor pointing at a corner reflector at around 30m

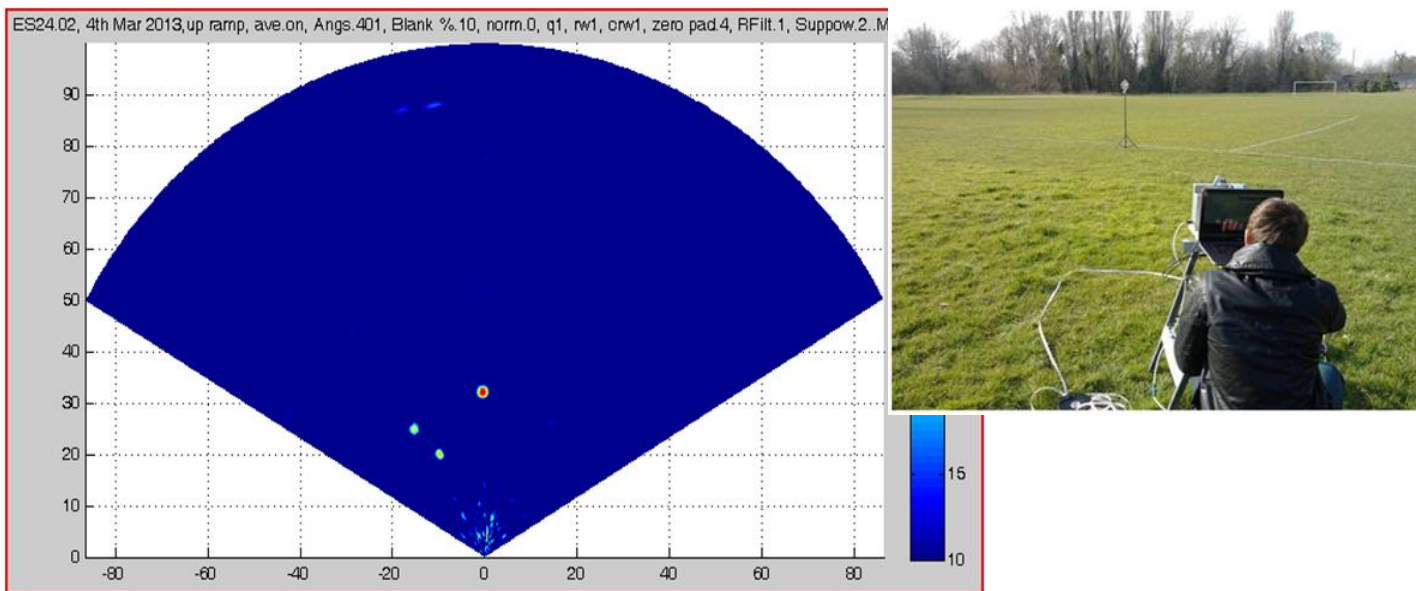


**Figure 5, Corner Reflector at 32m**

The corner reflector can clearly be seen on the radar plot at x0m, y32m. The two reflections to the left (approx. x-15m, y20m) are from the goalposts that are out of view in the photograph.

In order to investigate the range and angular resolution, look in detail at the results from the corner reflector at a range of 21m. Below shows the detail of the corner reflector with Hanning windows applied to both the range and angle.

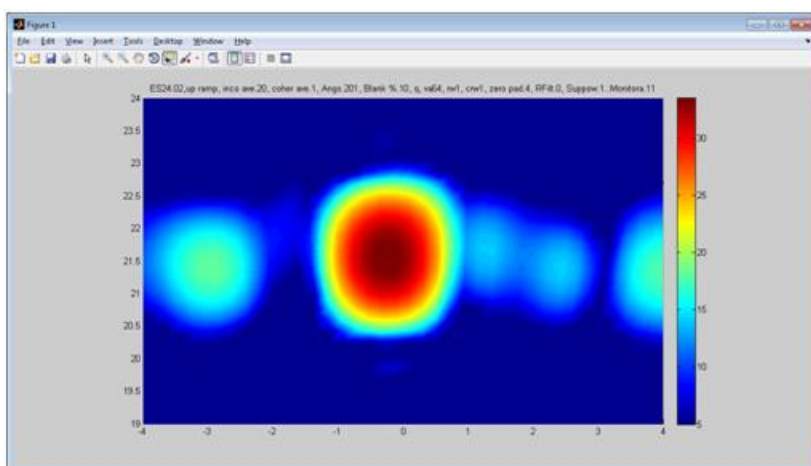


**Figure 6, Corner Reflector at 21m with Hanning Windows**

The windowing reduces the range and cross range side-lobes but at the expense of worsening the range and angle resolution as can be seen below which is the same image but with the windowing removed.

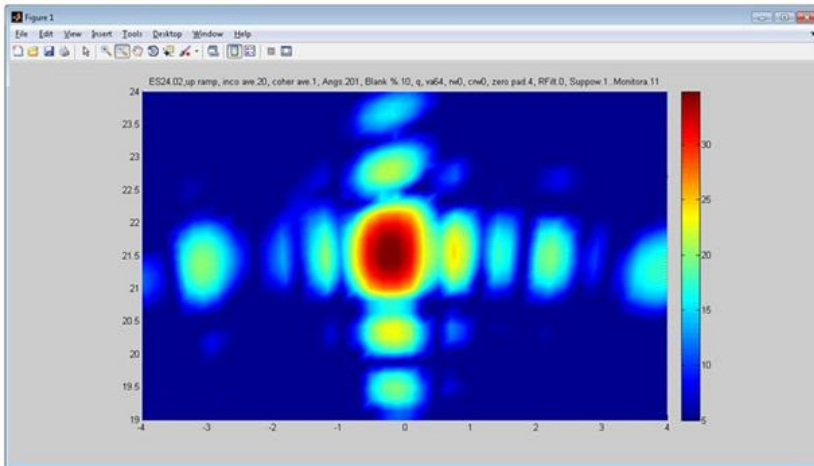


**Figure 7, Corner Reflector at 21m without windowing**

The target resolution is improved but at the expense of increased side-lobes. We will study the detail of the image without the windowing since this should be equivalent to the theoretical resolution calculated previously.

Below shows the target return as a function of range at a constant angle running through the peak of the signal.

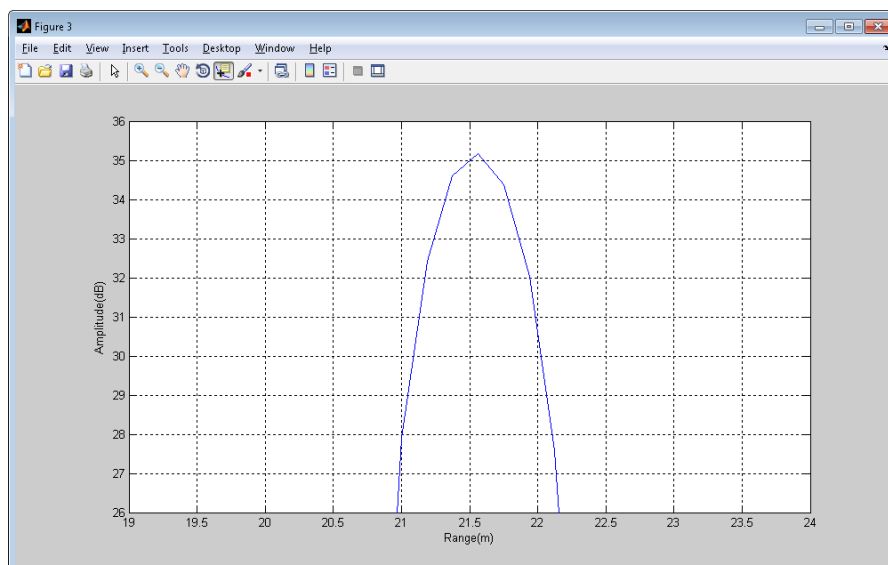


**Figure 8, Target Return Amplitude with Range**

The 3dB width of this is indeed around 0.75m as expected from the 200MHz chirp bandwidth.

Similarly, the graph below shows the target return as a function of angle at a fixed range running through the peak of the target return.

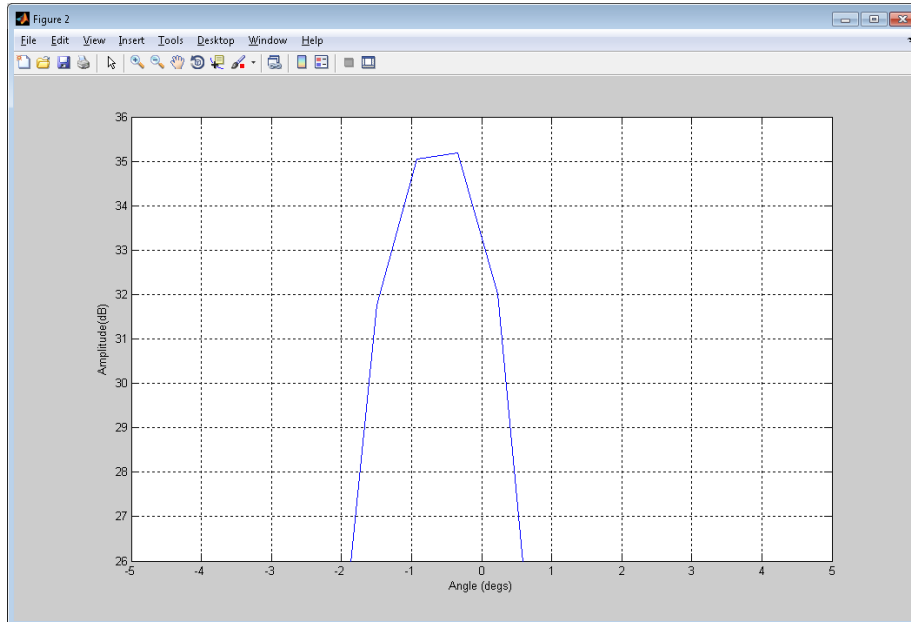


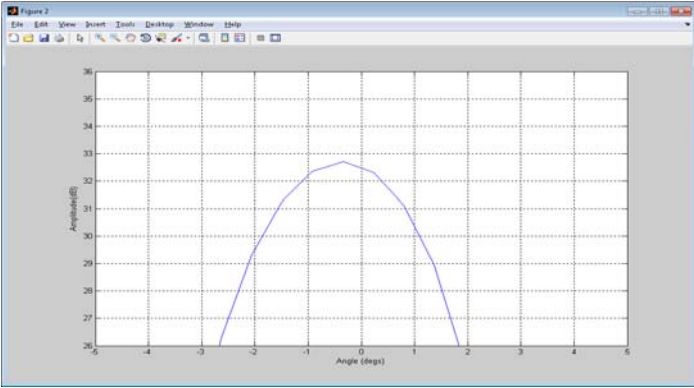
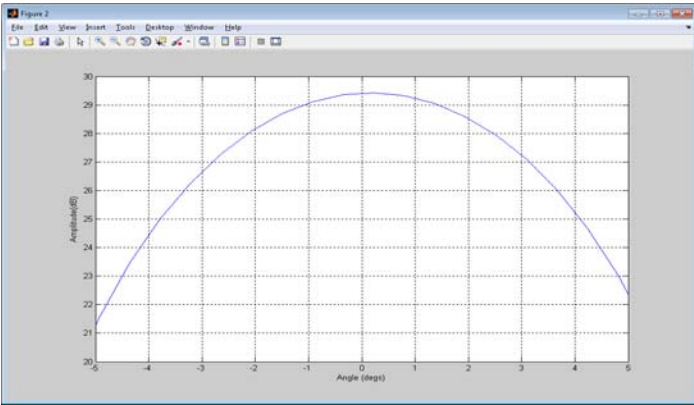
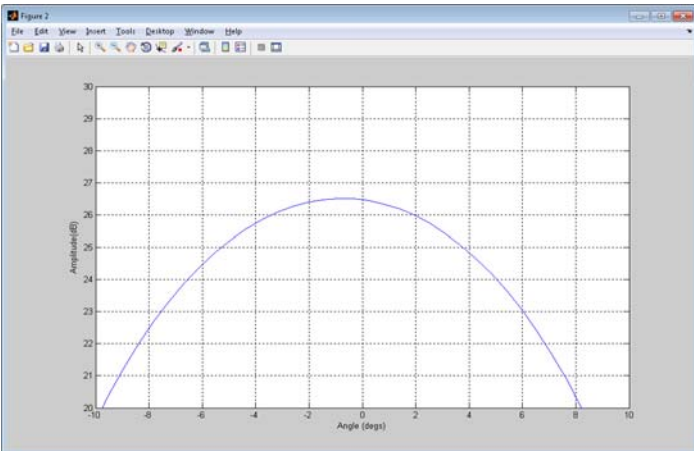
**Figure 9, Target Return Amplitude with Angle**

The 3dB width, again as predicted, is indeed around 1.8°.

With the Hanning windows, the range resolution increases to 1.2m and the angle resolution to 2.7°.



Since the signal from each virtual element is recorded separately, we can use fewer elements to generate the image and evaluate the effect this has on the angle resolution. This is illustrated in the figure below.

	Return with Angle	Resolution (degs)
32 Virtual Elements		3.3°
16 Virtual Elements		6.8°
8 Virtual Elements		13°

**Figure 10, Amplitude with Angle with Varying Number of Virtual Elements**

These results can be compared with the predicted results from earlier:

Number of Virtual Elements	8	16	32	64
Predicted Angular Resolution (Degrees)	16	7.6	3.7	1.8
Measured Angular Resolution (Degrees)	13	6.8	3.3	1.8

The figure below illustrates how the shape of the signal from a point source varies with range and cross range.

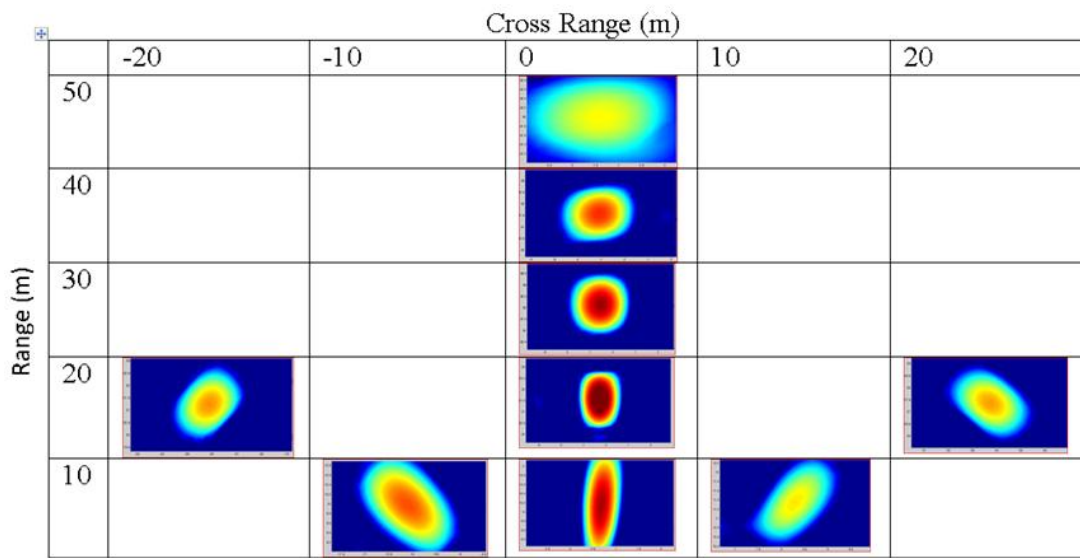
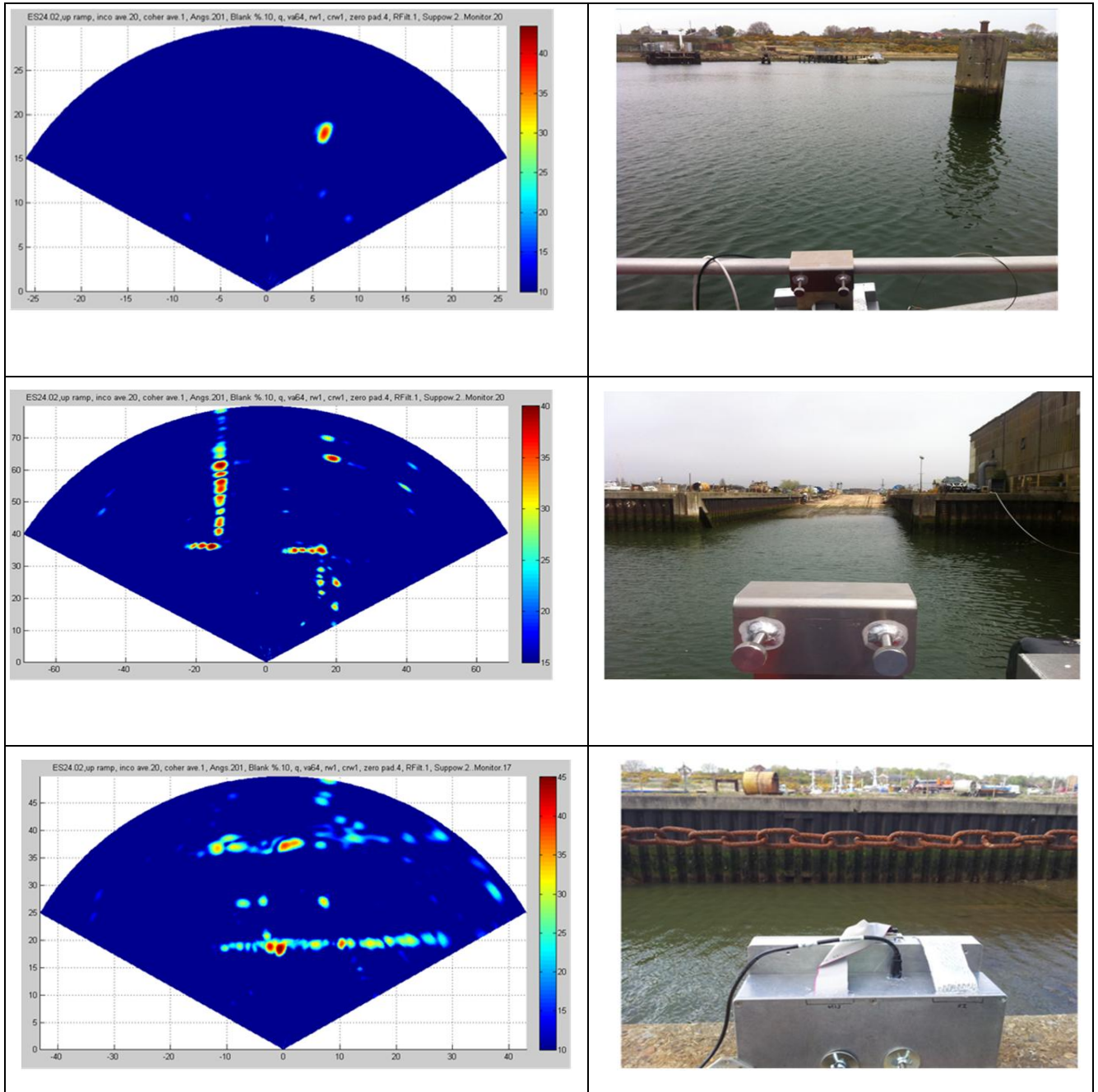


**Figure 11, Shape of Point Source with Varying Range and Cross Range**

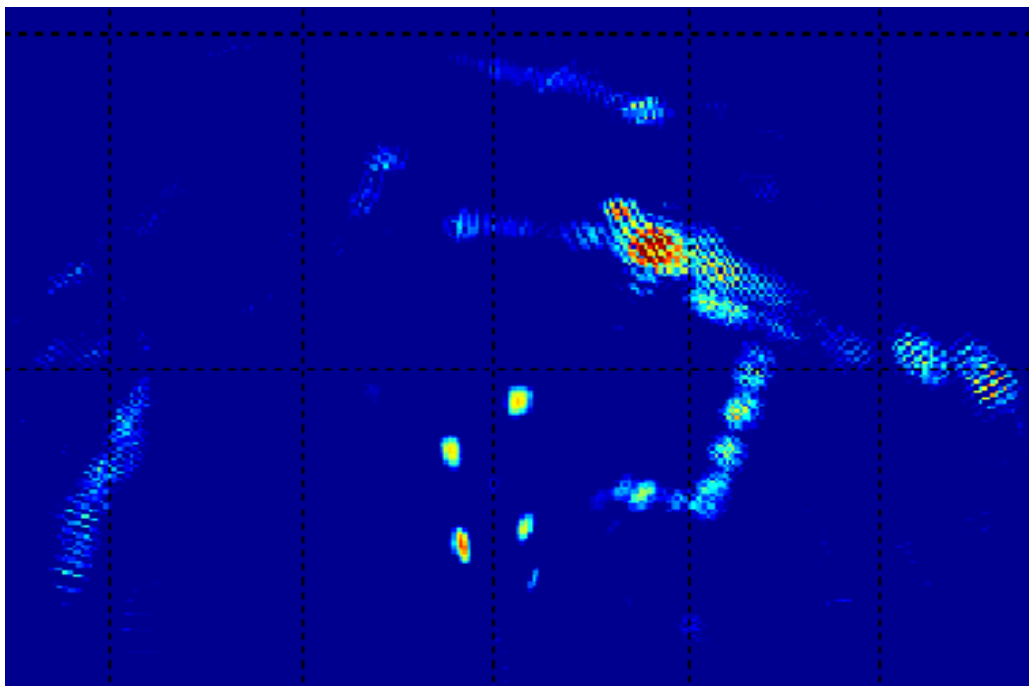
This shows that the range resolution is constant but the cross range resolution increases with range since it is a fixed angular resolution.

### 3.2 FIELD TRIAL RESULTS

The 24GHz radar has been taken out for field trials to see how it performs against various targets and scenes. The three images below are taken from a vessel at Lowestoft.



Below is an image of a car park with 6 small rocks which can be seen on by the radar.



## 4 CONCLUSIONS

In this paper, a novel MIMO array radar based on FMCW signals is described, from the physical MIMO array design to the signal model. The imaging processing theory has been derived and analyzed too to estimate the image quality. Some useful practices for designing the MIMO array and the waveform have been summarized as well and fulfilment of these guidelines ensure proper operation of the imaging radar.

A demonstration radar system based on a 4 TX and 16 RX array, operating at 24 GHz band, is therefore implemented using the theories derived. The same methodology can be used to design other linear arrays, at different frequencies, depending on the image resolution requirements and the available sampling rate.

As can be seen, the demonstrated image quality agrees very well with the theoretical expectation presented in the Section 2 of this paper. The range and angle resolutions have been measured to agree with those predicted. When this radar is used to image the surrounding environments, clear and accurate representations of the obstacles in the area monitored are seen from the radar image.

The compact and cost efficient MIMO array design is desirable in many new and promising applications. The compact structure of the antenna array does not require mechanical control and thus can be installed in places where it would be difficult for mechanical radar.

## 5 REFERENCES

- [1] E. Fishler, A. Haimovich, R. Blum, D. Chizhik, L. Cimini, and R. Valenzuela, "MIMO radar: an idea whose time has come", in *Radar Conference, 2004. Proceedings of the IEEE*, pp. 71-78, 2004.
- [2] Wulf-Dieter Wirth, *Radar techniques using array antennas*, the Institution of Electrical Engineers, 2001.
- [3] R. Schmidt, "Multiple emitter location and signal parameter estimation," *Antennas and Propagation, IEEE Transactions on*, vol. 34, no. 3, pp. 276-280, Mar.1986.
- [4] R. Roy, A. Paulraj, and T. Kailath, "Estimation of Signal Parameters via Rotational Invariance Techniques - ESPRIT", in *Military Communications Conference - Communications-Computers: Teamed for the 90's, 1986. MILCOM 1986. IEEE*, 3 ed p. 41, 1986.
- [5] P.Yang, F.yang, and Z.-P.Nie, "DOA estimation with sub-array divided technique and interpolated ESPRIT algorithm on a cylindrical conformal array antenna," *Progress In Electromagnetics Research*, vol. 103, pp. 201-216, 2010.
- [6] L. Jian, P. Stoica, and Z. Xiayu, "Signal Synthesis and Receiver Design for MIMO Radar Imaging," *Signal Processing, IEEE Transactions on*, vol. 56, no. 8, pp. 3959-3968, Aug.2008.
- [7] Y.Qu, G.Liao, S.-Q.Zhu, X.-Y.Liu, and H.Jiang, "Performance analysis of beamforming for MIMO radar," *Progress In Electromagnetics Research*, vol. 84, pp. 123-134, 2008.
- [8] J. H. G. Ender and J. Klare, "System architectures and algorithms for radar imaging by MIMO-SAR", in *Radar Conference, 2009 IEEE*, pp. 1-6, 2009.
- [9] J. H. G. Ender and J. Klare, "System architectures and algorithms for radar imaging by MIMO-SAR", in *Radar Conference, 2009 IEEE*, pp. 1-6, 2009.
- [10] P. Lacomme, J.-P. Hardange, J.-C. Marchais, and E. Normant, *Air and Spaceborne Radar Systems - An Introduction* William Andrew Publishing/Noyes, 2001.